Laser pulse dependent micro textured calcium phosphate coatings for improved wettability and cell compatibility

Sameer R. Paital · Wei He · Narendra B. Dahotre

Abstract Surface wettability of an implant material is an important criterion in biological response as it controls the adsorption of proteins followed by attachment of cells to its surface. Hence, micro-textured calcium phosphate coatings with four length scales were synthesized on Ti–6Al–4V substrates by a laser cladding technique and their effects on wettability and cell adhesion were systematically evaluated. Microstructure and morphological evolutions of the coatings were studied using scanning electron and light optical microscopes respectively. The surface texture of coating defined in terms of a texture parameter was correlated to its wetting behavior. The contact angle of simulated body fluid measured by a static sessile drop technique, demonstrated an increased hydrophilicity with decreasing value of texture parameter. The influence of such textures on the in vitro bioactivity and in vitro biocompatibility were studied by the immersion of the samples in simulated body fluid and mouse MC3T3-E1 osteoblast-like cell culture respectively.

1 Introduction

Bone graft procedures to heal skeletal defect is an area of active research as there exists millions of cases each year requiring such treatments [1]. These defects arise from several reasons including trauma, old age, congenital deformity, tumor resection, and injury and thus exist in a wide range of shapes, sizes, and functional locations [1]. The two most commonly used treatments to heal such defects are the autologous bone graft procedure and bone tissue engineering. Bone tissue engineering provides an attractive method than the autologous bone graft procedure as the latter is associated with the drawbacks such as limited supply of donor bone, risk of morbidity at the donor site, and risk of disease transmission and immune reaction arising from the donor site [2, 3]. The use of a solid artificial scaffold biomaterial that can support the bone cells and thereby provide anchorage for newly mineralized hard tissue is the most commonly used strategy for bone tissue engineering.

Among the various types of scaffold materials used, Hydroxyapatite (HA) and other calcium phosphate (CaP) bioceramics are being widely accepted owing to their similarity to the minerals in the natural bone, and their excellent bioactivity, biocompatibility, and osteoconduction [3–8]. When implanted inside a body these bioactive ceramics provide an ideal environment for cellular reaction, osteoblast colonization, and mineralized tissue integration to the implant surface. However, these CaP based ceramic materials possess inferior mechanical properties (low plasticity, fatigue, and creep resistance) and hence cannot be used as a stand alone implant material for hard tissue replacement. To overcome this issue, several researchers have emphasized on the coatings of CaP based bioceramics on titanium alloys [9–15]. Titanium being a bio-inert and biocompatible material, it does not elicit any harmful reaction and also provides appropriate mechanical properties for its long term stability inside the body. Hence, coating the surfaces of these implant materials (titanium alloys) by a CaP based chemistry can elicit favorable

S. R. Paital · W. He · N. B. Dahotre (✉)
Department of Materials Science and Engineering, The University of Tennessee, Knoxville, TN 37996, USA
e-mail: ndahotre@utk.edu

W. He
Department of Mechanical, Aerospace and Biomedical Engineering, The University of Tennessee, Knoxville, TN 37996, USA

biological and chemical responses on the surfaces, thereby enabling to mimic the reactions occurring in the natural tissue without losing the bulk mechanical properties such as long term durability and inertness.

The most commonly used coating technique that has been explored both in academic research and also largely practiced in the industry is the thermal spray coating technique [16]. However, this method suffers from certain drawbacks such as poor adherence of the coating to the substrate material, lack of uniformity of the coating, low fracture toughness of the ceramic layer, excess thickness of the coating, biodegradation, fatigue, third body wear, and absence of appropriate topographical cues mimicking the naturally occurring 3 dimensional extra cellular matrix (ECM) [16–18]. These attributes often result in loosening of the CaP ceramic coating due to non uniform load distribution and wear at the implant/defect tissue interface. The release of these foreign elements in the body environment can cause the problem of osteolysis. Further, the absence of appropriate topographical cues limits the anchoring of bone cells by contact guidance and hence, promotes weak bonding between the newly mineralized tissue and the scaffold material. The higher coating thickness (≥ 1 mm) associated with plasma spraying technique also poses a major problem as it can cause failure due to fatigue under tensile loading conditions [16]. Also with increasing thickness the residual stresses within the coating increase and corresponding energy release may promote cracking at the substrate/coating interface [16]. To address the above issues a variety of thin film-based coating techniques such as pulsed laser physical vapor deposition [19], magnetron sputtering [11], ion beam assisted deposition [10], etc. are being explored to deposit CaP coatings on metallic substrates. Nonetheless, none of these coating techniques is able to synthesize a sound metallurgical bonding between the CaP coating and the substrate and unable to create a regular three dimensional topographic cues on the surface. In order to improve the bonding strength between the coatings and the substrate, several researchers also tried upon the laser based melting technique [20–25]. In the work by Cheng and coauthors [20] a metallurgical bonding was achieved by directly melting the pre-placed HA-Ti composite powders on Ti alloy substrate using a Nd:YAG laser. The authors characterized the mechanical properties of the coatings using Vickers and nano indentation techniques. The higher values of hardness, elastic modulus and resistance to crack growth as obtained using the above techniques proved for the sound interfacial toughness of the coatings [20]. Lusquiños and co-authors [21, 22] used a laser based cladding technique where a high power laser beam was used to melt the substrate (Ti–6Al–4V), and a simultaneous jet of precursor (HA powder) was blown by a carrier gas on to the molten

cloud to form the coating. The authors showed the presence of a sound bonding and minimum dilution of the clad layer into the matrix of the substrate using SEM and XRD analysis of the cross-sectioned specimens [21]. A laser based cladding technique using calcium carbonate and calcium hydrogen phosphate as the precursor material to synthesize HA coating on Ti substrate was demonstrated by Wang et al. [23]. Using SEM and XRD analysis the authors showed the presence of sound bonding at the interface with cellular dendritic structure and consisting of phases HA, α-$Ca_2P_2O_7$, CaO and $CaTiO_3$ within the coating [23]. Although, all of the above works proved for the feasibility of a sound metallurgical bonding via laser based melting technique, none of these techniques could achieve a regular three dimensional topographic cue for contact guidance and adhesion of the bone cells.

In light of the above drawbacks associated with the present coating techniques, a laser based direct melting technique was established by the current group to simultaneously synthesize a textured CaP coating on Ti–6Al–4V substrate [26–30]. In the previous effort by the group [26, 28] a textured CaP coating on Ti–6Al–4V substrate was produced by direct melting of HA precursor using a continuous wave (CW) Nd:YAG laser. Here a systematic organization of the CaP coating on the Ti–6Al–4V substrate was obtained by effectively controlling the thermophysical interactions during laser processing. On the contrary, in the current work such feasibility of simultaneous synthesis of a textured CaP coating on Ti–6Al–4V substrate was realized using a pulsed Nd:YAG laser. During pulsed operation of Nd:YAG laser, the energy is delivered through intermittent pulses and hence the individual pulses can be controlled for duty cycle (on-off time), frequency (number of pulses delivered per second), and energy. Such control over selection of pulse parameters allows more precise control over spatial and temporal modes of delivery of laser energy, which in turn can create far more different thermal conditions, microstructures, and phase features within the laser-substrate interaction region than are obtained in the samples processed using a CW laser.

Further, wetting is an important aspect for all load bearing implants, as it controls the adsorption of proteins followed by attachment of cells to the implant surface. The surface morphology, surface chemistry, and surface charge of an implant material significantly influence its wetting behavior when it comes in contact with the physiological fluids under in vivo conditions [30]. An understanding of the mechanism of wetting will help in tailoring the surfaces for more hydrophilic behavior to physiological fluids and thereby help recruit proteins and bone cells from the surrounding to the implant surface swiftly. However, for the rough surface with irregular topographic cues the wetting dynamics is difficult to understand due to a non equilibrium

state of wetting and hence, no surface roughness parameters can be adopted to relate such a phenomenon. In light of this, with the present pulsed Nd:YAG laser coating technique, the sets of laser parameters can be chosen to synthesize surfaces with varying regular topographic cues. Finally, as the basis of the present study is to delineate and understand the effect of micro-textured surface morphology on wettability, in vitro bioactivity, and in vitro biocompatibility, the laser parameters are chosen to synthesize surfaces of the same phase composition and thereby only have a change in the surface topography.

2 Materials and methods

2.1 Sample preparation and Ca–P coating

Ti–6Al–4V substrate coupons (100 mm × 50 mm × 3 mm) cut from the rolled sheets were polished using 30 μm grit SiC emery paper followed by rinsing with acetone. The HA ($Ca_{10}(OH)_2(PO_4)_6$)) powder (Fisher Scientific, USA) was used as the precursor material. This precursor powder had a spherical morphology with a unimodal distribution in the range of 10–30 μm. The precursor was mixed with a water-based organic solvent LISI W 15853 (Warren Paint and Color Company, Nashville, TN, USA) and sprayed onto the substrate coupons using an air pressurized spray gun. This green body was air dried to remove the moisture and a uniform thickness of 80 μm was maintained for all precoating precursor deposits. The samples were then scanned using a 400 W average power, JK701 model pulsed Nd:YAG laser to obtain the coating. The schematic of the laser coating experimental set up used for the coating process is shown in Fig. 1. The processing parameters used for the above process are listed in Table 1. From the table it can be observed that
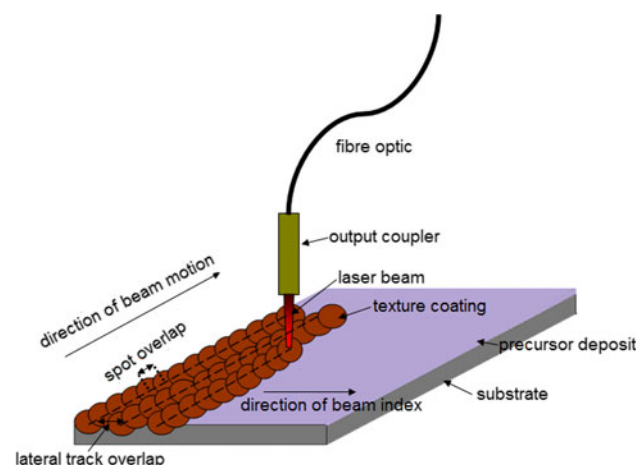
Fig. 1 Schematic of laser texturing process using pulsed Nd:YAG laser

Table 1 Laser parameters used in the study

Pulse width	1 ms
Pulse energy	4 J
Pulse repetition rate	10, 20, 30, 40 Hz
Laser scan speed	50 cm min^{-1}
Focus position	0.8 mm above sample surface
Spot diameter on the surface	900 μm
Pulse shape	Rectangular

only the laser pulse frequency was varied (10, 20, 30, and 40 Hz) keeping the rest of the parameters constant. This pulse frequency can be related to the spot overlap by the following equation [29, 30]:

$$(\text{Spot diameter}) \times (1 - \text{spot overlap}) \times (\text{pulse frequency})$$
$$= \text{linear scan speed.} \qquad (1)$$

Hence, four different samples with spot overlap varying as 6, 53, 69 and 76% were obtained.

2.2 Surface characterization

The morphological evolutions of the surface of the coatings were characterized using low magnification Leica optical microscopes. The microstructure within the cross-section and the morphological evolution of the surface of coatings following immersion in a simulated body fluid (SBF) were characterized using a LEO 1525 scanning electron microscope (SEM). The samples in cross-section were prepared by polishing with emery papers of different grits ranging from 200 to 1,000 μm in succession followed by disc polishing with colloidal silica of 0.3 and 0.05 μm. The polished samples were then cleaned with acetone and etched with 5 vol% HF, 3 vol% HNO_3 and 92 vol% H_2O for 10–20 s by immersion etching to delineate the microstructural features.

Phase evolution within the coatings was studied using a Philips Norelco X-ray diffractometer (XRD) with Cu K_α radiation of wavelength 1.5418 Å. The system was operated at 20 kV and 10 mA in a 2θ range of 20° to 100° using a step size of 0.02° and count time of 1 s. In order to correlate the effects of surface roughness to wettability two roughness parameters such as standard deviation of amplitude (σ_A) and wavelength (λ) of the textured surface were measured using the Leica confocal laser microscope. Eventually, their ratio (σ_A/λ) defined as the texture parameter is used to reveal the effect of surface morphology on wettability. A total of 5 random scans were chosen on each sample and the sampling showed that the parameters can be defined with an accuracy of 2–4%.

2.3 Contact angle and in vitro bioactivity

Wettability of the coated samples with SBF was carried out by a static sessile drop technique using a CAM-Plus^R contact angle goniometer (Cheminstruments, Inc. Fairfield, Ohio) equipped with a fiber optic light source and Video camera for imaging. Prior to the contact angle measurements the samples were thoroughly cleaned with acetone and air dried. The SBF solution was prepared by mixing reagent grade chemicals in the following order: NaCl (8.026 g), NaHCO$_3$ (0.352 g), KCl (0.225 g), K$_2$HPO$_4$·3H$_2$O (0.230 g), MgCl$_2$·6H$_2$O (0.311 g), CaCl$_2$ (0.293 g) and Na$_2$SO$_4$ (0.072 g) into distilled water (700 ml). The fluid was then buffered to pH = 7.4 at 37°C with tri-hydroxymethyl-aminomethane (6.063 g) and hydrochloric acid (40 ml). A SBF droplet of volume 3 μl (droplet diameter of 2 mm) was placed on the thoroughly cleaned sample by a hypodermic syringe and the advancing contact angle was recorded as a measure of wettability. The liquid drop placed on the sample was allowed to stabilize for 10 s before the reading was taken. The test was conducted at room temperature (26°C) and a minimum of 10 contact angle readings were taken on each sample to minimize errors in the measurement. Further, the measurements were based on the patented half angle method (US Patent 5268733) which eliminates the errors associated with the arbitrary tangential alignment.

In vitro bioactivity and mineralization on the laser processed samples were studied by immersing a set of four samples from each processing condition in the SBF solution. Plastic containers were used to soak the samples in SBF for different time periods (24, 72, 120, and 168 h). The solution was refreshed every 24 h to maintain a pH of 7.4, and the temperature was maintained at 37°C during the course of the test. The samples were removed at regular intervals from the SBF solution and an increase in weight owing to the precipitation of HA was measured using a microbalance. The change in pH of the SBF solution was monitored using a Fisher Scientific FB-10 pH meter.

2.4 In vitro biocompatibility

In vitro biocompatibility of laser textured samples and control (untreated Ti–6Al–4V) was evaluated through cell attachment and cell morphology during cell culture studies using the mouse pre-osteoblast MC3T3-E1 (subclone 14) cell line, obtained from American Type Cell Culture Collection (ATCC, Manassas, VA, USA). The cells were maintained in a tissue culture flask using the cell culture medium at 37°C under 5% CO$_2$ and 95% air in a humidified incubator. The cell culture medium used in the present case was Alpha minimum essential medium (Invitrogen Corporation, USA) supplemented with 10% fetal bovine serum (Thermo Fisher Scientific Inc, USA) and 1% penicillin/streptomycin (Invitrogen Corporation, USA). The culture medium was replaced every 3 days and confluent cells were trypsinized and replated (0.25% trypsin-EDTA, Invitrogen, USA) to maintain the cell line.

2.4.1 Cell morphology and cell cytoskeleton

The osteoblast cells suspended in 300 μl cell culture medium were seeded on the UV sterilized samples at a lower density (1 × 10^4 cells cm^{-2}) and incubated for 24 and 168 h at 37°C under 5% CO$_2$ and 95% air in a humidified incubator. For cell morphology analysis using SEM, cells cultured on the samples were fixed with 3% glutaraldehyde in 0.1 M cacodylate for 1 h and rinsed three times with phosphate buffered saline (PBS). The samples were further processed in 2% osmium tetroxide in 0.1 M cacodylate for 1 h, dehydrated with a series of increasing concentration of ethanol (25, 50, 70, 95, and 100%), critical point dried, and sputter-coated with gold for SEM observation. For immunocytochemical staining of the actin filament and focal adhesion, the cells cultured on the samples were fixed with 4% paraformaldehyde (Sigma-Aldrich, USA) in 1× PBS for 30 min at 4°C. After washing with PBS, the samples were permeabilized with 0.1% Triton X-100 (Fisher Scientific, USA) in 1× PBS for 5 min, blocked with 1% bovine serum albumin (BSA, Sigma-Aldrich, USA) for 30 min, and incubated in the primary antibody mouse anti-vinculin (Chemicon, 0.2%) for 1 h. After rinsing, the samples were incubated with 0.5% goat anti-mouse IgG Alexa Fluor 488 and 2% Alexa Fluor 594-conjugated phalloidin (Invitrogen, USA) that labels the cytoskeleton F-actin filaments. Cell nuclei were counterstained with 0.1% 4′,6-Diamidino-2-phenylindole (DAPI, Chemicon, USA) in 1× PBS for 5 min. Samples were washed three times with 0.05% Tween-20 (Sigma) in 1× PBS before and after the staining steps. All the staining procedures were carried out at room temperature. High resolution fluorescence images were captured using an upright fluorescence microscope (Nikon). Once the images were captured, a representative image was selected for quantitative analysis of cell spreading area (A), and cell shape index (Ø). A total of 30 cells were randomly selected for each sample, manually outlined, and the cell areas (A) were calculated using the ImageJ image analysis software. The morphology of the cells described by the cell shape index (Ø) was calculated using the following equation [31]:

$$\varnothing = \frac{4\pi A}{p^2}. \tag{2}$$

Here A is the cell spreading area and p the perimeter of the cell. For a perfect circular morphology the cell shape index is 1, whereas for line morphology the shape index is 0.

Previous studies [32] have demonstrated a correlation between the cell shape index and cell fate and function, thereby offering the potential to tailor biomaterial surfaces to control cell fate and function through control of cell spreading.

2.4.2 Data analysis

For a particular time period of seeding a total of 4 samples were used from each laser processing parameters and the control (untreated Ti–6Al–4V). The results were expressed as the mean of 4 replicates $\pm$ SD (standard deviation). Statistical analysis carried out using a Student's t test was applied to determine the statistical significance observed between the groups and $P < 0.05$ were considered statistically significant.

3 Results and discussions

### 3.1 Microstructure, morphology, and phase analysis

The low-magnification optical microscopic images (Fig. 2) of the surfaces of laser textured samples clearly demonstrate the effect of varying laser pulse frequency on the texture evolution. The laser pulse frequency influences the input energy density [29], and the laser spot overlap as indicated by Eq. 1. Each single pulse of a laser beam on the surface of sample produces a solidified crater with a defined boundary and central flat region. Hence, when such craters are overlapped by varying the laser pulse frequency, surfaces with varying textures are obtained. Further, with increasing pulse frequency, the input energy density increases and this in turn also contributes to the texture evolution. The presence of such geometrically textured cues is expected to support bone cells and thereby induce bone in-growth from the surrounding tissue. The cross-sectional SEM image (Fig. 3a) of the sample processed at 40 Hz is clearly an indicative of the sound metallurgical bonding between the coating and the substrate (Ti–6Al–4V). A sound bonding of the bioceramic coating to the substrate material is expected to reduce the delamination of the ceramic layer and thereby avoid the risk of dissolving metallic ions into the body plasma and the problem of osteolysis.

The variable thermodynamic conditions resulting from the varying pulse frequency within the range employed in the present work only influenced the texture evolution and no detectable variation in the evolution of types of phases (Fig. 3b) is observed. The major phases identified within the detectable limits of the instrument are $Ca_{10}(PO_4)_6(OH)_2$, $CaTiO_3$, TiO_2 (Rutile and Anatase), $Ca_3(PO_4)_2$, and Al_2O_3.
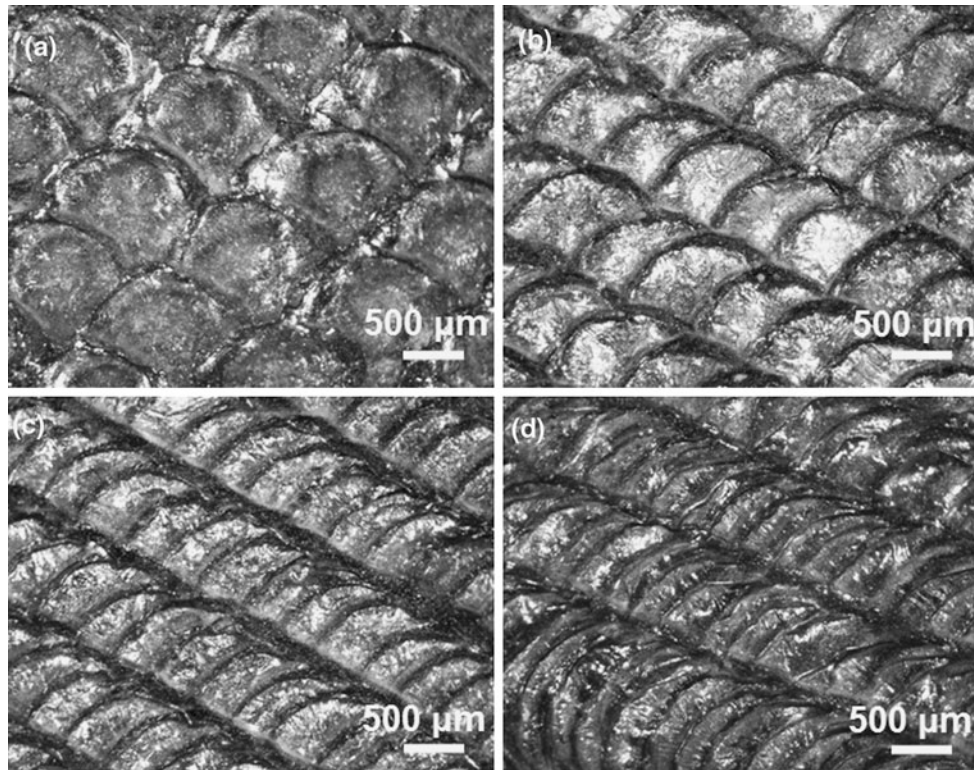
Fig. 2 Low-magnification optical microscopic images of the surface of coatings processed at laser pulse frequencies of **a** 10 Hz, **b** 20 Hz, **c** 30 Hz, and **d** 40 Hz
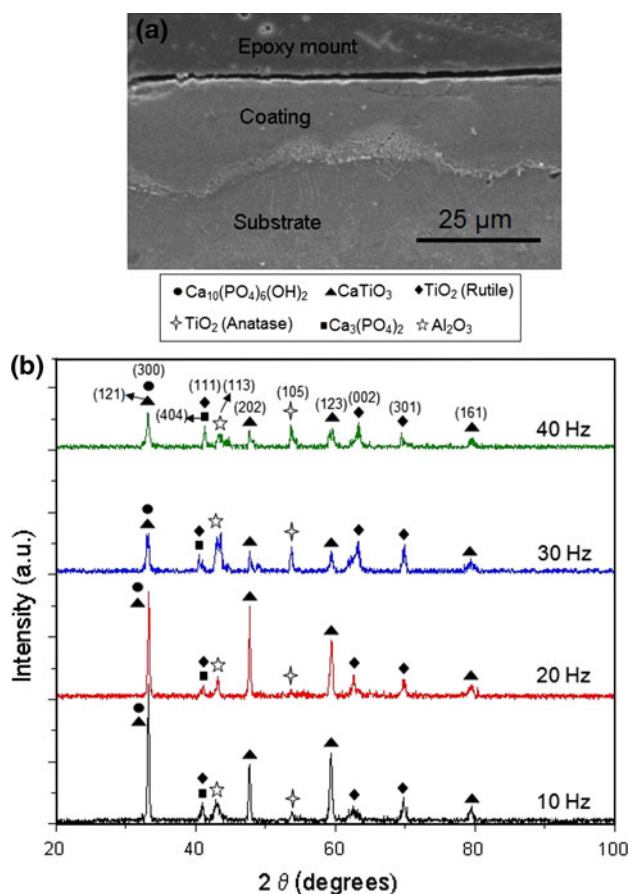
Fig. 3 **a** Cross-sectional SEM images of the sample processed at 40 Hz and **b** XRD pattern for the laser processed samples at varying pulse frequencies

Although, there is no major variation in the types of phases evolved, the variation in peak intensities is clearly an indication of the variation in amounts of these phases with increasing pulse frequency. As the pulse frequency was increased from 10 to 40 Hz there is a decrease in peak intensities of $Ca_{10}(PO_4)_6(OH)_2$ and $CaTiO_3$ phases along (300) and (123) planes respectively (Fig. 3b). Also, with increasing pulse frequency there is an increase in peak intensities of the TiO_2 (Rutile) and TiO_2 (Anatase) phases along (002) and (105) planes respectively. The above observations can be attributed to the fact that with increase in laser pulse frequency from 10 to 40 Hz, there was an increase in the laser input energy density. Such increased input energy was likely to raise the temperature of laser material interaction zone to the level leading to the substantial amount of coating precursor material evaporation followed by oxidation of the substrate material for formation of more amount of TiO_2 and Al_2O_3. Although the identical phases are present in the coatings of all laser processed samples, as stated in the following sections, during SBF immersion, these samples with varying surface topographic cues demonstrated varying

wetting response and significant hydrophilicity with SBF compared to uncoated Ti–6Al–4V.

3.2 Effects of phase and morphology on wettability

The effect of laser pulse frequency (within the range employed in the present study) on three dimensional surface morphology of the coatings recorded using a confocal laser microscopy is presented in Fig. 4a. The sample processed at 10 Hz possesses a relatively rough morphology compared to the samples processed at 20, 30, and 40 Hz. As described earlier, due to only 6% overlap associated with 10 Hz frequency, the craters produced were least affected by the subsequent pulses. On the contrary, the frequencies of 20, 30, and 40 Hz provided substantially increased overlap of 53, 69, and 76% respectively. This increased spot overlap resulted in re-melting of the major portion of prior crater leading to smoothening of the coating. The values of σ_A, λ, and their ratio σ_A/λ were obtained from 5 random locations on each sample and are presented as mean values with related scatter in Table 2. All laser processed samples are associated with a significantly smaller value of σ_A/λ compared to the control (untreated Ti–6Al–4V). Also for all laser processed samples, with an increase in pulse frequency (in the range employed in the present study) there is a decrease in the σ_A/λ value. This further agrees with earlier visual observations that an increasing surface smoothening creeps in with increasing pulse frequency.

It has been well established that wetting of a surface by liquid is significantly affected by its surface roughness [30, 33]. The chart in Fig. 4b provides the experimental contact angles subtended by the SBF drop on laser processed samples and the control Ti–6Al–4V. All laser processed samples except the sample processed at 10 Hz depict an improved hydrophilic behavior compared to the control Ti–6Al–4V. Among the laser processed samples, the sample processed at 40 Hz possesses the maximum hydrophilicity to SBF with a contact angle of approximately 40°. The shadow image of SBF droplet (Fig. 4b) also shows the spreading of the SBF drop on the samples processed at 40 Hz. Thus, there is a decrease in the experimental contact angle with decreasing texture parameter (σ_A/λ) (Table 2; Fig. 4b). This improved hydrophilic behavior of laser processed samples is attributed to the influence of surface texture and the types of phases (HA, $CaTiO_3$, $Ca_3(PO_4)_2$, TiO_2 (Anatase), and TiO_2 (Rutile)) evolved during laser processing.

The wettability of laser processed sample, and the correlation between texture parameter (σ_A/λ) and experimental contact angle can be explained as per the wetting model on rough surfaces described by Zhou and De Hosson [33]. According to their model a practical rough surface is

Fig. 4 a The 3-dimensional confocal microscopic images of surface of the coatings and **b** contact angle variation and their corresponding shadow images of the SBF droplet on laser processed sample and control (untreated Ti–6Al–4V)
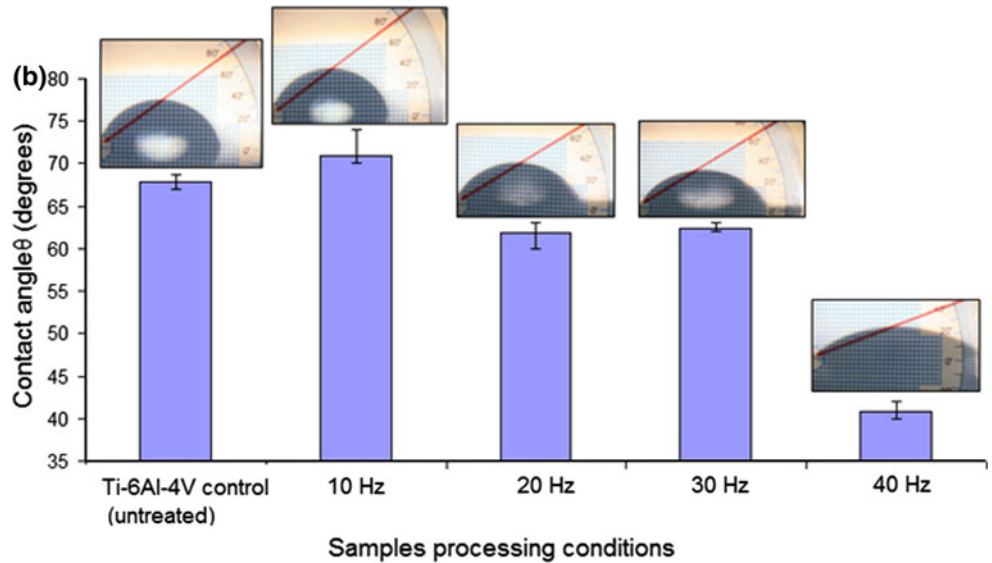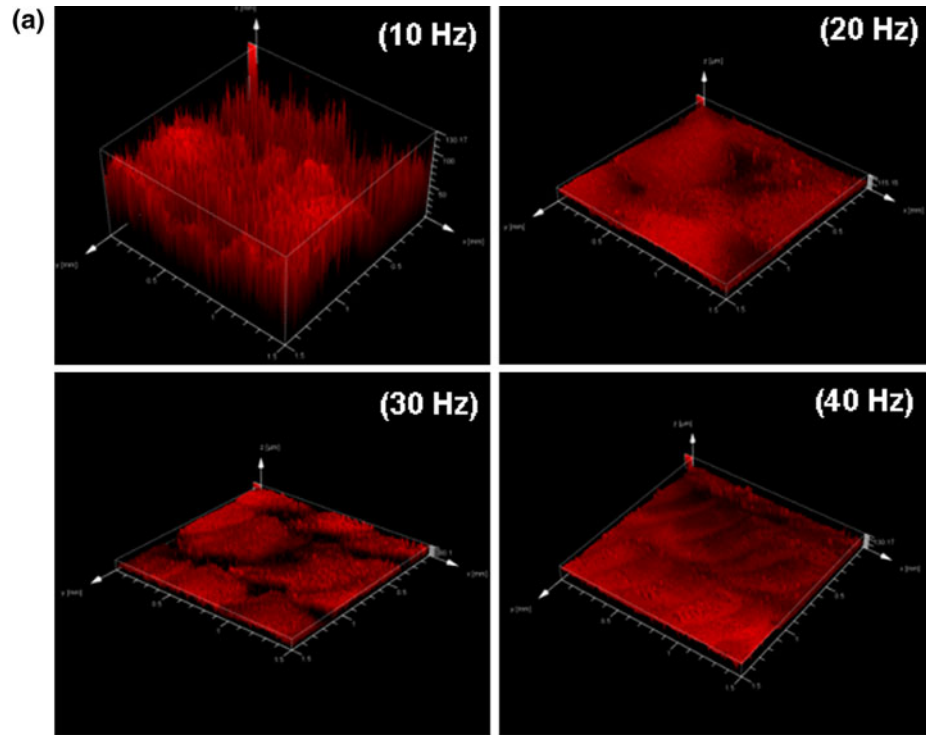
Table 2 Experimentally measured physical parameters related to surface texture

| Sample	Frequency (Hz)	Standard deviation of amplitude σ_A (µm)	Wavelength λ (µm)	Texture parameter (σ_A/λ)
Bare Ti–6Al–4V	–	12.56 ± 0.17	2.79 ± 0.08	4.38 ± 0.04
Ti–6Al–4V/Ca–P	10	23.05 ± 0.023	0.9 ± 0.016	0.05655 ± 0.016
Ti–6Al–4V/Ca–P	20	19.41 ± 0.014	0.6 ± 0.104	0.0385 ± 0.0101
Ti–6Al–4V/Ca–P	30	15.4 ± 0.01235	0.4 ± 0.1095	0.03235 ± 0.026
Ti–6Al–4V/Ca–P	40	11.31 ± 0.018	0.2 ± 0.0125	0.025655 ± 0.016
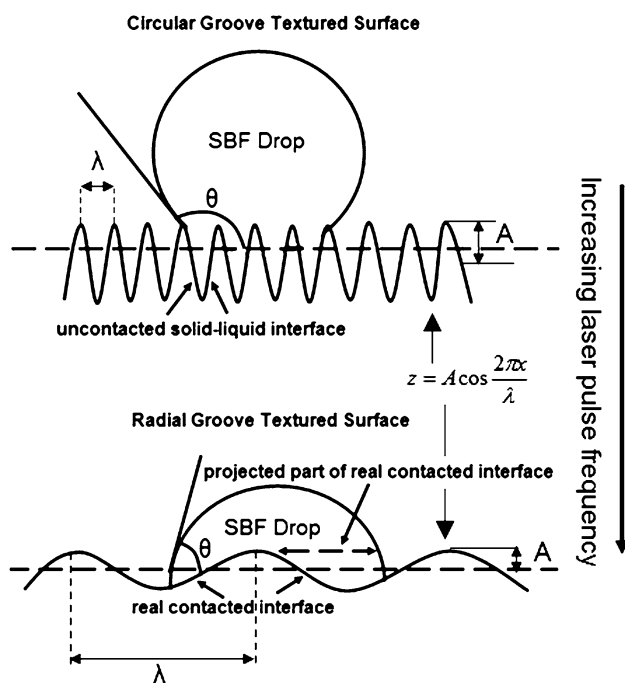
Fig. 5 Schematic of the wetting behavior of a liquid drop on a surface with **a** the circular grooves and **b** the radial grooves

assumed to have a cosine profile (Fig. 5) with a Gaussian distribution and is either of a radial or circular type grove. When a liquid is placed on the surface with only radial type groves, an equilibrium state of wetting is achieved and the relation between the experimental contact angle affected by the radial groves (θ_{rad}) and the theoretical contact angle (θ_{th}) is given by the following equation [33]:

$$\cos\theta_{rad} = D(1 - F)\cos\theta_{th} - F \qquad (3)$$

where D is defined as the average area ratio of real contacted interface to its projected part, and F is the area fraction of an uncontacted solid–liquid interface on solid. The theoretical contact angle θ_{th} is defined as: $\cos\theta_{th} = (\gamma_S - \gamma_{LS})/\gamma_L$ where γ_S, γ_{LS}, and γ_L are the interface energies between solid–vapor, liquid–solid, and liquid–vapor interfaces respectively. For a radial groove, both D and F are constants and since, the rough surface is assumed to distribute as a cosine profile with a Gaussian distribution, they are both a function of σ_A/λ [33]. Hence, when a liquid drop is placed on such surface (smaller σ_A/λ value) it can easily overcome the energy barriers associated with it and completely wet it. Thus, an equilibrium state of wetting and thereby a smaller experimental contact angle is observed
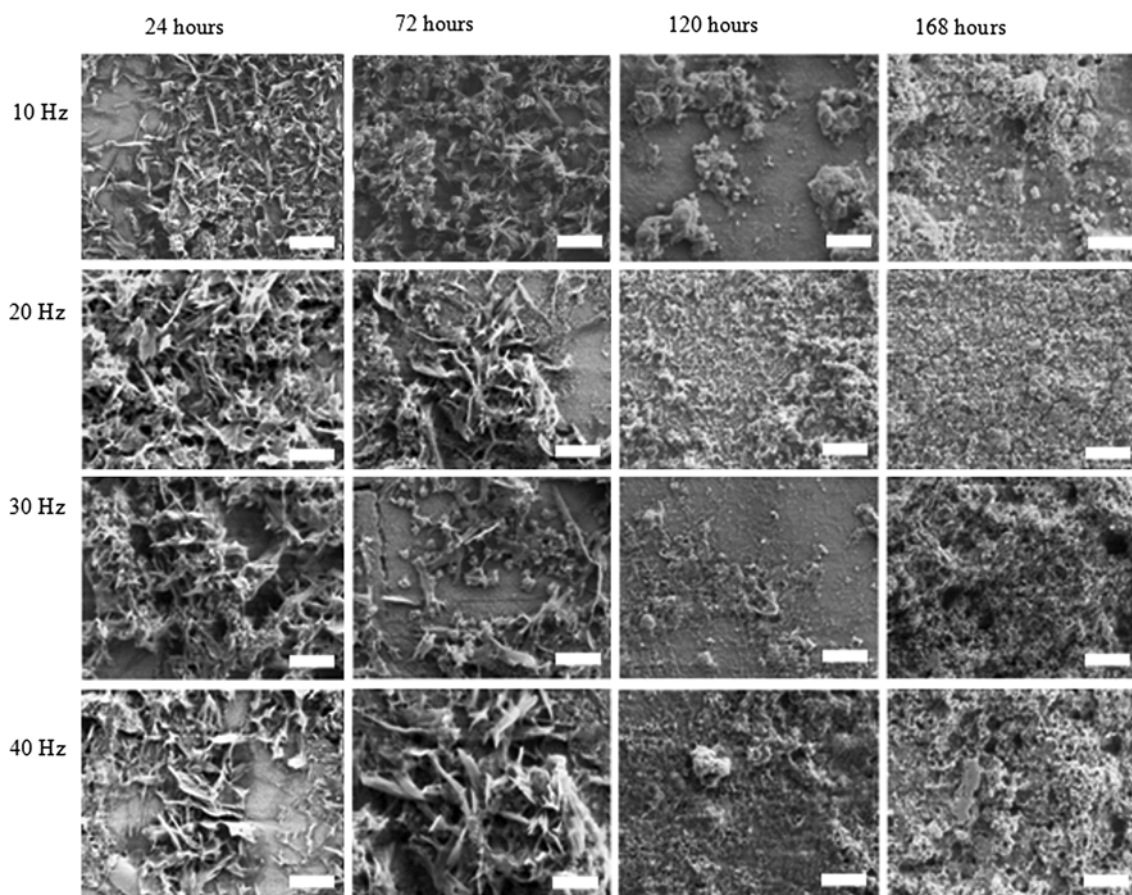
Fig. 6 SEM micrographs of laser processed samples following immersion in SBF for different time periods. *Scale bar* in the figure is equivalent to 10 μm

Fig. 7 XRD spectra of laser textured samples following immersion in SBF for various immersion periods
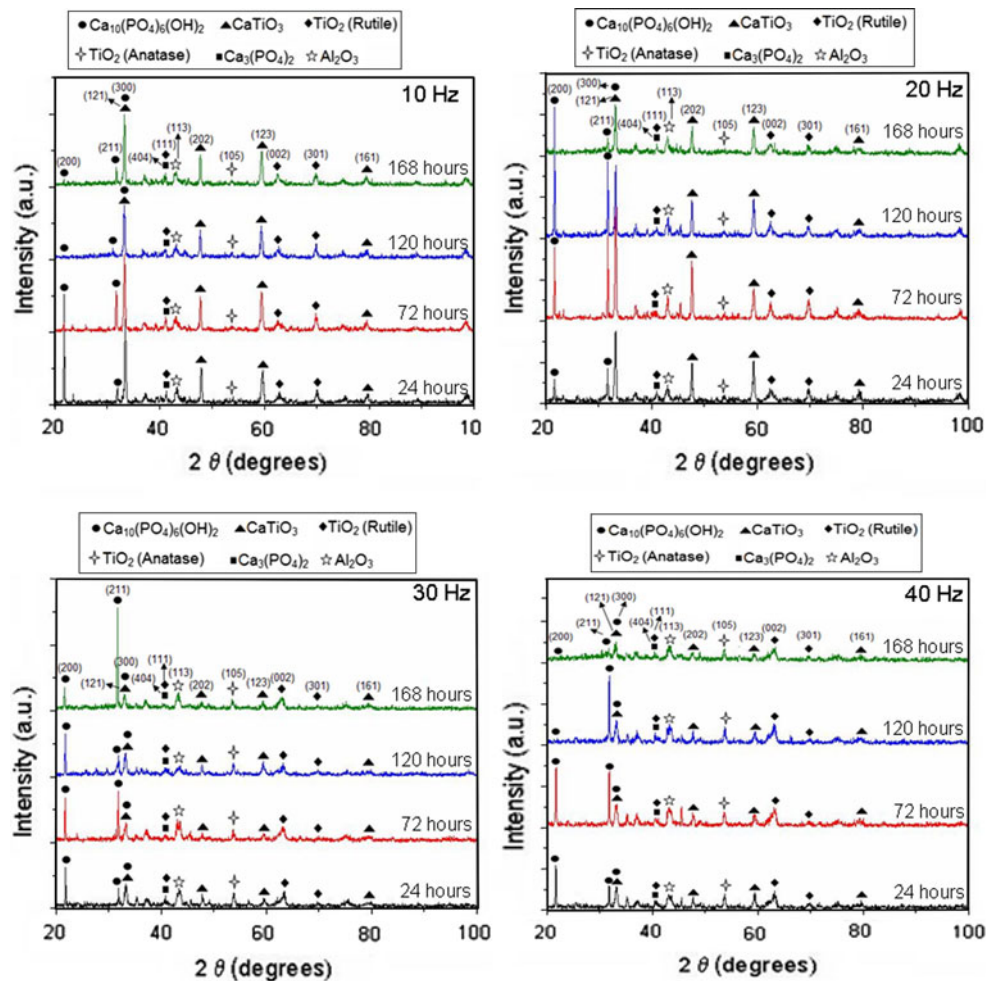
when the grooves are radial. In contrast, when the surface possesses sharp circular type features (higher σ_A/λ value) an equilibrium state of wetting could never be achieved. This type of sharp feature with higher σ_A/λ value contributes to the contact angle hysteresis and the experimental contact angle affected by these kinds of grooves (θ_{cir}) can be related to theoretical contact angle (θ_{th}) by the following equation:

$$\theta_{cir} = \theta_{th} + \left(\frac{\sqrt{8\pi}}{\lambda}\sigma_A\right). \tag{4}$$

From the above equation it is clear that a sharp circular type groove with higher σ_A/λ value can only result in a higher contact angle and thereby a reduced wettability. Hence, from the above equations based on the model by Zhou and De Hosson, optical microscopy observations (Fig. 2a), and confocal microscopy images (Fig. 4a) it is clearly evident that at a laser pulse frequency of 10 Hz and associated minimal spot overlap produced a deep and circular groove morphology on the surface. This in turn resulted in a higher σ_A/λ value, leading to unstability in wetting and increased contact angle as per Eq. 4. However, when the pulse frequency increased to 20, 30, and 40 Hz

there was increased remelting due to increased spot overlap which in turn resulted in a relatively smoothly textured surface with lower σ_A/λ values. Therefore, the samples processed at these higher pulse frequencies are dominated by radial grooves that lead to improved wettability. As stated earlier, wetting is an important phenomenon which influences the mineralization, cell attachment, and cell proliferation. In light of this, the above preliminary efforts and corresponding understanding are further used to see how the texture parameter and associated wettability affect in vitro bioactivity and in vitro biocompatibility.

3.3 In vitro bioactivity and mineralization

In vitro bioactivity of laser textured samples and control (untreated Ti–6Al–4V) was assessed for precipitation of an apatite (HA, [$Ca_{10}(PO_4)_6(OH_2)$]) like mineral layer on the surface during immersion in SBF. The precipitation of such phase under in vivo conditions is beneficial as HA is a naturally occurring mineral component of the human bone laying along side the collagen fibrils. This layer, therefore, provides an appropriate surface chemistry for cell
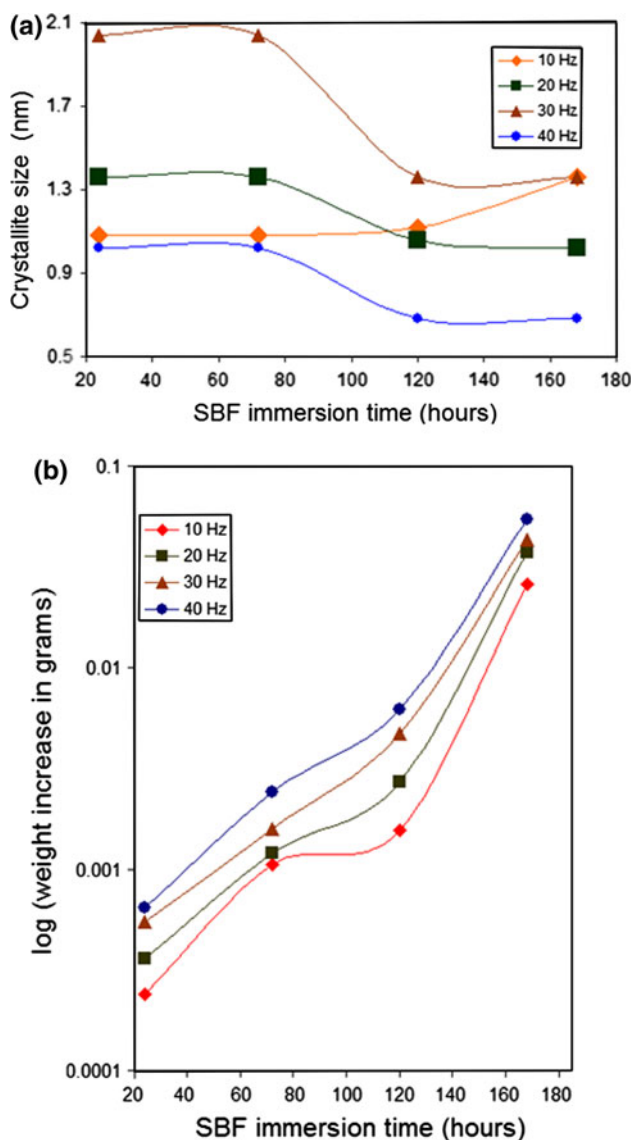
Fig. 8 Mineralization of laser textured samples in terms of **a** variation in apatite crystallite size with SBF immersion time and **b** logarithmic weight change with SBF immersion time

attachment and proliferation and minimizes the formation of a fibrous capsule at the interface.

As, there was no detectable amount of HA precipitation on the control (untreated Ti–6Al–4V) following 24 h of immersion in SBF, the SEM and XRD results pertaining to it are not included in the present study. However, the laser textured surfaces demonstrated the precipitation of a whisker-like apatite phase (Fig. 6) soon after 24 h of immersion in SBF. The presence of such morphology is attributed to heterogeneous nucleation of the hexagonal close packed (HCP) apatite crystal (on the substrate material) and subsequent growth of this HCP structure along the *c* axis (perpendicular to the close packed atomic plane) by the adsorption of Ca^{2+} and PO_4^{3-} ions from the

super-saturated SBF solution. For longer immersion times this equilibrium morphology (whisker like apatite phase) due to its surface energy and modified Ca^{2+} and PO_4^{3-} ions concentration within the surrounding SBF solution in turn control the further nucleation process and thereby the change in morphology of the newly precipitated apatite crystals. Irrespective of the laser processing conditions (varying σ_A/λ value) a transition from whisker-like apatite phase to refined submicron size HA with increasing immersion time are observed in all samples (Fig. 6). To better understand the structural change in the apatite phase with increasing immersion time, XRD studies were carried out on the SBF immersed samples and the crystallite size (S) in a direction perpendicular to the surface of the specimen were measured from a highly resolved apatite peak using the Scherrer equation:

$$S = \frac{0.9\lambda}{\beta \cos \theta} \tag{5}$$

where λ is the wavelength of the X-ray source (1.54 A), θ is the half of the reported peak centroid and β is the broadening or the full width half maxima (FWHM) of the reported peak.

XRD studies of all laser textured samples following immersion in SBF for different time periods, indicated the presence of an apatite phase as evident from the characteristic HA peaks at $2\theta \sim 22.0°$ and $31.75°$ corresponding to the planes (200) and (211) respectively (Fig. 7). All samples (irrespective of the processing parameters and varying σ_A/λ value) following 24 h of immersion in SBF, demonstrated intense peaks at $2\theta \sim 22.0°$ and $31.75°$ that are attributable to the apatite phase. However, with increased immersion time these apatite peaks are either broadened with a reduction or sharpened with an increase in intensity. To precisely understand this phenomenon and thereby its influence on the crystallite size the highly resolved apatite peak corresponding to the plane (211) at $2\theta \sim 31.75°$ was used for calculations in Eq. 5. Figure 8a shows the variation in apatite crystallite size with increasing SBF immersion time for all laser textured samples. All laser textured samples except the sample processed at 10 Hz experience decrease in the apatite crystallite size with increasing SBF immersion time (Fig. 8a). For the sample processed at 40 Hz, precipitated apatite crystallites were the smallest and the average crystallite size was approximately 1.02 nm during the first 72 h of SBF immersion time, and decreased to 0.6795 nm as the immersion time is increased to 120 and 168 h. The precipitation of such submicron size crystallites may be due to increased heterogeneous nucleation sites of the ionic species (Ca^{2+} and PO_4^{3-} ions from the SBF) on the substrate material owing to its improved wettability. This in turn may have resulted in reduction of Ca^{2+} and
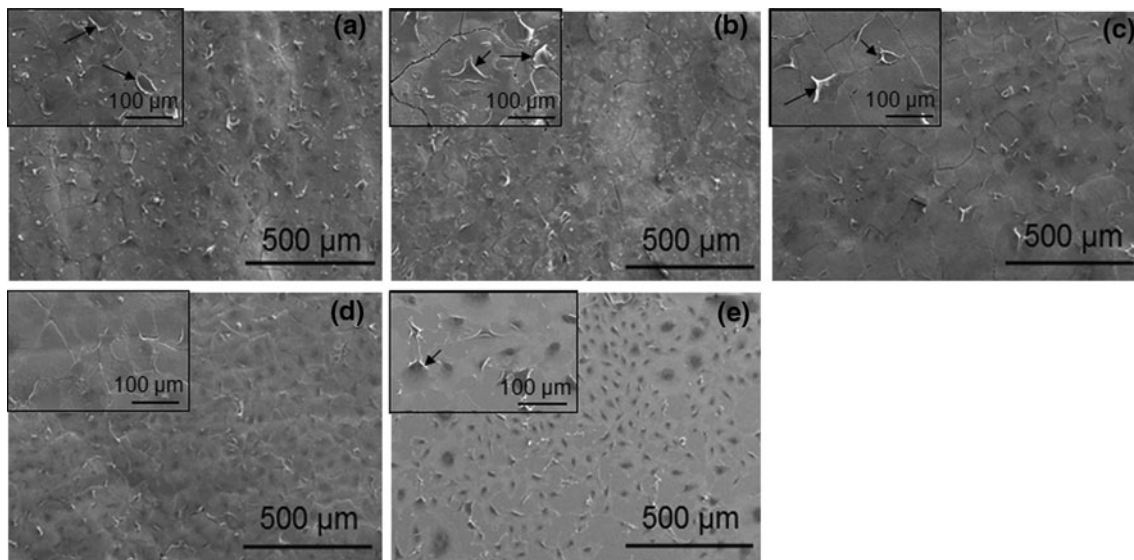
Fig. 9 Morphology of MC3T3-E1 osteoblast-like cells after 7 day culture on the samples processed at laser pulse frequency of **a** 10 Hz, **b** 20 Hz, **c** 30 Hz, **d** 40 Hz and **e** control (untreated Ti–6Al–4V).

Arrows in the inset of Fig. 9**a**, **b**, **c**, and **e** indicate the de-bonding or lack of proper adhesion of the MC3T3-E1 osteoblast-like cells on the substrate material

PO_4^{3-} ions concentration in the SBF leading to the growth arrest of HCP habit plane. On the contrary, the reduced hydrophilic nature of 10 Hz sample may have resulted in the less number of heterogeneous nucleation sites and hence the availability of more Ca^{2+} and PO_4^{3-} ions from SBF to nucleate on to the apatite crystal.
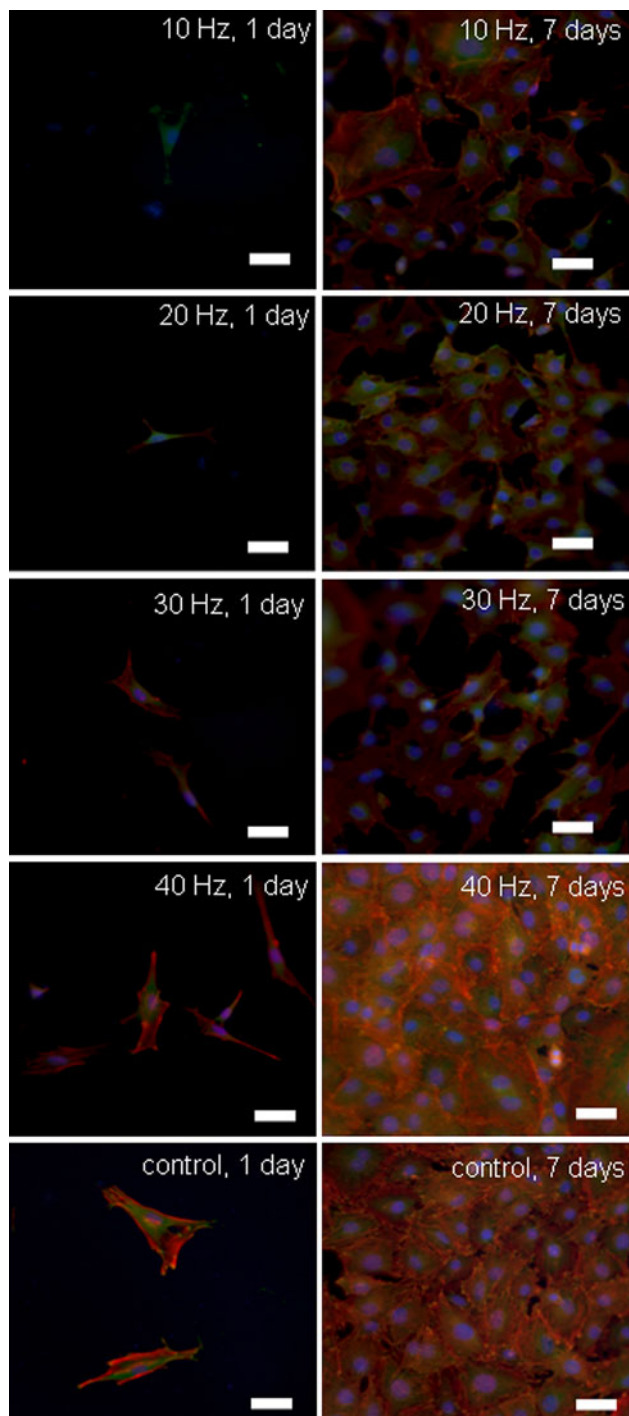
It is well known that as the apatite nucleation takes place under in vitro conditions, it modifies the initial surface layer and this in turn can control the subsequent precipitation. Hence, it would be interesting to study the mineralization behavior in terms of weight change with increasing SBF immersion time. The logarithmic weight increase with increasing SBF immersion time for all the laser processed samples is presented in Fig. 8b. Also, as observed in our earlier work [30] as well as in the present study, the mineralization on the control (untreated Ti–6Al–4V) was not of detectable amount, hence its mineralization behavior with increasing SBF immersion time is not included in the present study. The mineralization increased with increasing SBF immersion time and followed the same trend for all laser textured samples with varying σ_A/λ values. Also, with an increase in pulse frequency (decrease in σ_A/λ value) there is an increase in HA precipitation for each SBF immersion time and the sample processed at 40 Hz (smaller σ_A/λ value) experienced the maximum weight change. This improved mineralization on laser processed samples is attributed to improved wettability (Fig. 4b) as a result of the appropriate surface textures (smaller σ_A/λ value, Table 2) and the types of phases (HA, $CaTiO_3$, $Ca_3(PO_4)_2$, TiO_2 (Anatase), and TiO_2 (Rutile), Fig. 3b) evolved during laser processing. Also, as

described earlier, among all laser processed samples the precipitates formed on the sample processed at 40 Hz were the smallest for all immersion times (Fig. 8a). The presence of such smaller crystallites provides increased surface energy for increased nucleation of HA on the surface of sample and thereby improves its mineralization under in vivo conditions.

3.4 Biocompatibility assessment

Cell morphology on laser processed and control (untreated Ti–6Al–4V) samples after 7 day culture of MC3T3-E1 osteoblast-like cells was assessed by SEM and the results are presented in Fig. 9. Surfaces of all laser processed samples (Fig. 9a, b, c, and d) and the control (untreated Ti–6Al–4V, Fig. 9e) were confluent with the MC3T3-E1 osteoblast-like cells after 7 day of culture period. However, for the control (untreated Ti–6Al–4V) and samples processed at 10, 20, and 30 Hz most of the osteoblast-like cells appeared to de-bond from the surface of the coatings. In contrast, the osteoblast-like cells appeared to be flattened, spread out uniformly, and strongly adhered with an elliptical and circular morphology on the sample processed at 40 Hz.

The proliferation of the osteoblast-like cells after 1 and 7 day of culture on the laser processed and control (untreated Ti–6Al–4V) samples were studied qualitatively using a fluorescence microscope (Fig. 10). After 1 day of culture there are very few cells in the image fields of all laser processed samples and the control (untreated Ti–6Al–4V). The MC3T3-E1 osteoblast-like cells have a triangular

Fig. 10 Fluorescence microscopic images showing the proliferation of the MC3T3-E1 osteoblast-like cells after 1 and 7 day of culture on the laser processed and control (untreated Ti–6Al–4V). *Scale bar* in the figure is equivalent to 50 μm

at 40 Hz, the osteoblast-like cells are more confluent with well stressed actin filaments and are very much comparable to the control (untreated Ti–6Al–4V).

The cytoskeletal organization of the MC3T3-E1 osteoblast-like cells on the control (untreated Ti–6Al–4V) and laser processed samples after 7 days culture are presented in Fig. 11a. All the samples indicate stressed actin filaments with well developed network of focal adhesion contacts. Also it can be qualitatively observed that for the sample processed at 40 Hz, the foot print area or the cell spreading is relatively more compared to the rest of laser processed samples and control (untreated Ti–6Al–4V). The cell shape index (after 7 days culture of MC3T3-E1 osteoblast-like cells), calculated using the cell spreading area (A) and the perimeter (p) of the cell, provided a higher value for the sample processed at 40 Hz (Fig. 11b) as compared to the control (untreated Ti–6Al–4V) and the sample processed at 10, 20, and 30 Hz. This, therefore, indicated the uniform spreading and circularity of the osteoblast-like cells on the sample processed at 40 Hz.

Although all laser processed samples (10, 20, 30, and 40 Hz) produced the same types of phases (HA, $CaTiO_3$, $Ca_2(PO_4)_2$, TiO_2 (Rutile), and TiO_2 (Anatase)) and physical textures with smaller values of σ_A/λ on the surface for substantially improved wettability compared to the control (untreated Ti–6Al–4V), only the sample processed at 40 Hz demonstrated reasonably improved biocompatibility in terms of cell morphology, cell proliferation, and cell shape index compared to the control. Thus these observations indicate that in general, the processing approach holds a promise in producing the attributes (surface composition and surface texture) suitable for improved biocompatibility. In light of this, the efforts are on going to explore and extend the laser processing parameters for a larger matrix to produce samples of substantially improved biocompatibility. Further, long term cell culture studies in terms of cell viability and cell differentiation are in the process to understand its biocompatibility and the results pertaining to the above will be discussed in our subsequent journal communications.

4 Conclusions

The laser direct melting of HA precursor on the Ti–6Al–4V substrate resulted in formation of various phases such as, $CaTiO_3$, $Ca_3(PO_4)_2$, TiO_2 (Anatase), and TiO_2 (Rutile), within the coated regions. By varying the laser pulse frequency in combination of appropriate selection of other laser processing conditions only a variation in surface morphology was achieved keeping the phase composition same. The sample processed at a laser pulse frequency of 40 Hz is associated with a smallest texture parameter (σ_A/λ) leading to the maximum wettability with SBF. This

morphology with the lamellipodia trying to extend along the surface of sample. In contrast, after 7 days of culture, the osteoblast-like cells are confluent over the entire surfaces of all samples and exhibit either elliptical or polygonal like morphology. Especially, for the sample processed
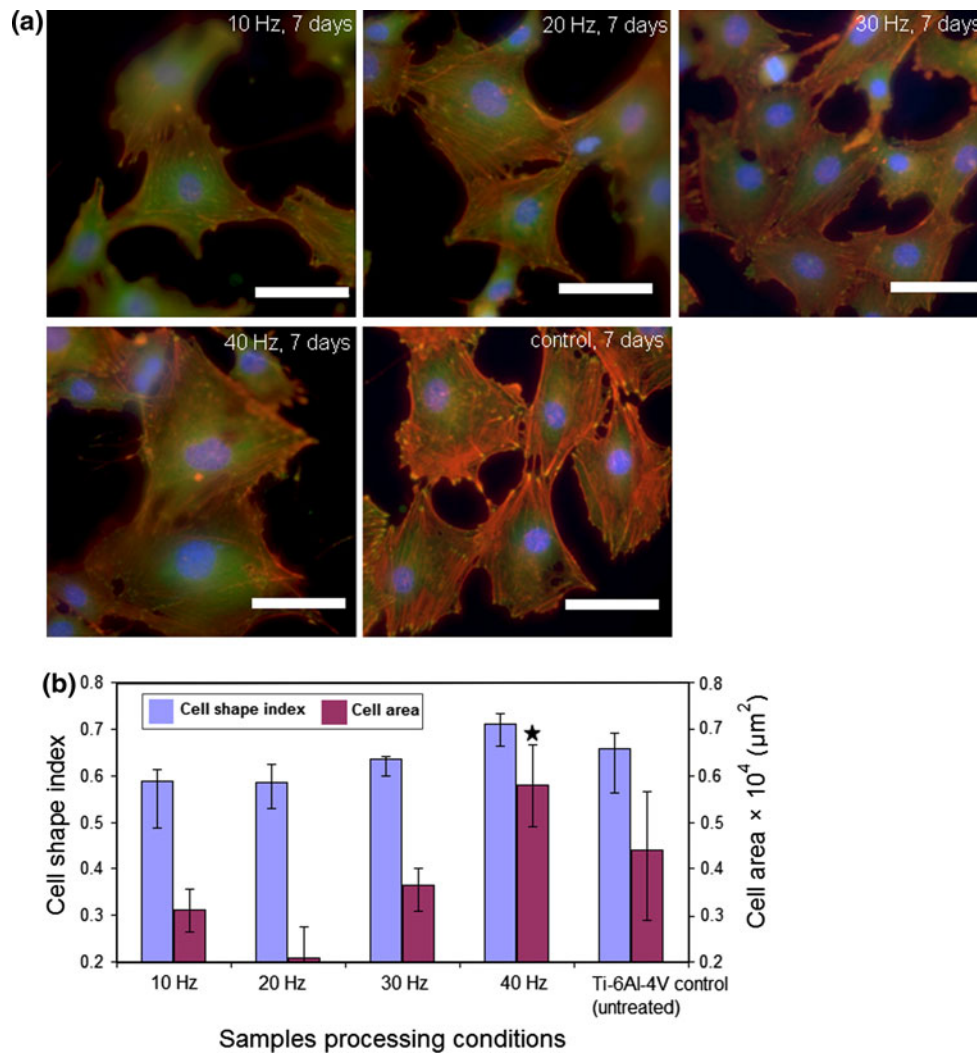
Fig. 11 a Cytoskeleton assessment of the MC3T3-E1 osteoblast-like cells after 7 day culture on the laser processed samples and the control (untreated Ti–6Al–4V) and **b** cell shape index and cell area as a function of the samples processing conditions. *Scale bar* in the figure is equivalent to 50 μm and ★ denotes the laser processed processed group is significantly higher than the control

improved hydrophilic behavior for the sample processed at 40 Hz also resulted in its enhanced mineralization (in vitro bioactivity) following immersion in SBF and improvement in in vitro biocompatibility characterized via increased proliferation and spreading of the MC3T3-E1 osteoblast-like cells.

References

1. Fisher JP. Tissue engineering. 1st ed. New York: Springer; 2006. p. 225.

2. Zhang ZY, Teoh SH, Chong WS, Foo TT, Chng YC, Choolani M, Chan J. A biaxial rotating bioreactor for the culture of fetal mesenchymal stem cells for bone tissue engineering. Biomaterials. 2009;30:2694–704.

3. Quan R, Yang D, Yan J, Li W, Wu X, Wang H. Preparation of graded zirconia-CaP composite and studies of its effect on rat osteoblast cells in vitro. Mater Sci Eng C. 2009;29:253–60.

4. Moreau JL, Xu HHK. Mesenchymal stem cell proliferation and differentiation on an injectable calcium phosphate-chitosan composite scaffold. Biomaterials. 2009;30:2675–82.

5. Mei HH, Phillips GJ, Mikhalovsky SV, Lloyd AW. In vitro cytotoxicity assessment of carbon fabric coated with calcium phosphate. New Carbon Mater. 2008;23:139–43.

6. Baker KC, Drelich J, Miskioglu I, Israel R, Herkowitz HN. Effect of polyethylene pretreatments on the biomimetic deposition and adhesion on calcium phosphate films. Acta Biomater. 2007; 3:391–401.

7. Chou L, Marek B, Wagner WR. Effect of hydroxyapatite coating crystallinity on biosolubility, cell attachment efficiency and proliferation in vitro. Biomaterials. 1999;20:977–85.

8. Alcaide M, Serrano MC, Pagani R, Salcedo SS, Regi VM, Portoles MT. Biocompatibility markers for the study of interactions between osteoblasts and composite biomaterials. Biomaterials. 2009;30:45–51.

9. Shih WJ, Wang SH, Li WL, Hon MH, Wang MC. The phase transition of calcium phosphate coatings deposited on a Ti–6Al–4V substrate by an electrolytic method. J Alloys Compd. 2007;434–435:693–6.

10. Blalock T, Bai X, Rabiei A. A study on microstructure and properties of calcium phosphate coatings processed using ion beam assisted deposition on heated substrates. Surf Coat Technol. 2007;201:5850–8.

11. Boyd AR, Meenan BJ, Leyland NS. Surface characterization of the evolving nature of radio frequency (RF) magnetron sputter deposited calcium phosphate thin films after exposure to physiological solution. Surf Coat Technol. 2006;200:6002–13.

12. Wen HB, de Wijin JR, van Blitterswijk CA, de Groot K. Incorporation of bovine serum albumin in calcium phosphate coating on titanium. J Biomed Mater Res. 1999;46:245–52.

13. Ji H, Ponton CB, Marquis PM. Microstructural characterization of hydroxyapatite coating on titanium. J Mater Sci: Mater Med. 1992;3:283–7.

14. Habibovic P, Barrère F, van Blitterswijk CA, de Groot K, Layrolle P. Biomimetic hydroxyapatite coating on metal implants. J Am Ceram Soc. 2002;85:517–22.

15. Ramires PA, Romito A, Cosentino F, Milella E. The influence of titania/hydroxyapatite composite coatings on in vitro osteoblasts behavior. Biomaterials. 2001;22:1467–74.

16. Paital SR, Dahotre NB. Calcium phosphate coatings for bio-implant applications: materials, performance factors, and methodologies. Mater Sci Eng: R: Rep. 2009;66:1–70.

17. Campbell AA, Fryxell GE, Linehan JC, Graff GL. Surface-induced mineralization: a new method for producing calcium phosphate coatings. J Biomed Mater Res. 1996;32:111–8.

18. Gracía-Sanz FJ, Mayor MB, Arias JL, Pou J, León B, Pérez-Amor M. Hydroxyapatite coatings: a comparative study between plasma-spray and pulsed laser deposition techniques. J Mater Sci: Mater Med. 1997;8:861–5.

19. Clèries L, Fernández-Pradas JM, Morenza JL. Bone growth on and resorption of calcium phosphate coatings obtained by pulsed laser deposition. J Biomed Mater Res. 2000;49:43–52.

20. Cheng GJ, Pirzada D, Cai M, Mohanty P, Bandyopadhyay A. Bioceramic coating of hydroxyapatite on titanium substrate with Nd:YAG laser. Mater Sci Eng C. 2005;25:541–7.

21. Lusquiños F, Pou J, Arias JL, Boutinguiza M, Pérez-Amor M, León B, Driessens FCM. Production of calcium phosphate coatings on Ti6Al4V obtained by Nd:yttrium-aluminum-garnet laser cladding. J Appl Phys. 2001;90:4231–6.

22. Lusquiños F, De Carlos A, Pou J, Arias JL, Boutinguiza M, León B, Pérez-Amor M, Driessens FCM, Hing K, Gibson I, Best S, Bonfield W. Calcium phosphate coatings obtained by Nd:YAG laser cladding: physicochemical and biologic properties. J Biomed Mater Res. 2003;64A:630–7.

23. Wang D, Chen C, Ma J, Zhang G. In situ synthesis of hydroxyapatite coating by laser cladding. Colloids Surf B: Biointerfaces. 2008;66:155–62.

24. Roy M, Krishna BV, Bandyopadhyay A, Bose S. Laser processing of bioactive tricalcium phosphate coating on titanium for load-bearing implants. Acta Biomater. 2008;4:324–33.

25. Zhang Y, Gao J, Tan J, Zou Z. Laser surface coating of a bioceramic composite layer. Surf Coat Technol. 1993;58:125–7.

26. Kurella A, Dahotre NB. Laser induced hierarchical calcium phosphate structures. Acta Biomater. 2006;2:677–88.

27. Kurella A, Dahotre NB. A multi-textured calcium phosphate coating for hard tissue via laser surface engineering. J Miner, Met Mater Soc (JOM). 2006;58:64–6.

28. Paital SR, Dahotre NB. Laser surface treatment for porous and textured Ca–P bio-ceramic coating on Ti–6Al–4V. Biomed Mater. 2007;2:274–81.

29. Paital SR, Balani K, Agarwal A, Dahotre NB. Fabrication and evaluation of a pulse laser-induced Ca–P coating on a Ti alloy for bioapplication. Biomed Mater. 2009;4:1–10.

30. Paital SR, Dahotre NB. Wettability and kinetics of hydroxyapatite precipitation on a laser-textured Ca–P bioceramic coating. Acta Biomater. 2009;5:2763–72.

31. Palson BØ, Bhatia SN. Tissue engineering. 1st ed. New Jersey: Pearson Prentice Hall; 2004. p. 252–5.

32. Chen CS, Mrksich M, Huang S, Whitesides GM, Ingber DE. Geometric control of cell life and death. Science. 1997;276:1425–8.

33. Zhou XB, De Hosson JThM. Influence of surface roughness on the wetting angle. J Mater Res. 1995;10:1984–92.